Received: 9 March 2020 | Revised: 26 May 2020 | Accepted: 5 June 2020

DOI: 10.1096/fj.202000566R

RESEARCH ARTICLE

THE FASEB JOURNAL

Human riboflavin kinase: Species-specific traits in the biosynthesis of the FMN cofactor

Ernesto Anoz-Carbonell[1,2] | **Maribel Rivero**[1] | **Victor Polo**[2,3] | **Adrián Velázquez-Campoy**[1,2,4,5,6] | **Milagros Medina**[1,2]

[1]Departamento de Bioquímica y Biología Molecular y Celular, Facultad de Ciencias, Universidad de Zaragoza, Zaragoza, Spain

[2]Instituto de Biocomputación y Física de Sistemas Complejos (GBsC-CSIC and BIFI-IQFR Joint Units), Universidad de Zaragoza, Zaragoza, Spain

[3]Departamento de Química Física, Universidad de Zaragoza, Zaragoza, Spain

[4]Fundación ARAID, Diputación General de Aragón, Zaragoza, Spain

[5]Aragon Institute for Health Research (IIS Aragon), Zaragoza, Spain

[6]Biomedical Research Networking Centre for Liver and Digestive Diseases (CIBERehd), Madrid, Spain

Correspondence
Milagros Medina, Departamento de Bioquímica y Biología Molecular y Celular, Facultad de Ciencias, Pedro Cerbuna 12, Universidad de Zaragoza, 50009-Zaragoza, Spain.
Email: mmedina@unizar.es

Funding information
Spanish Ministry of Economy, Industry and Competitiveness, Grant/Award Number: BIO2016-75183-P AEI/FEDER; Spanish Ministry of Science and Innovation, Grant/Award Number: PID2019-103901GB-I00 AEI/FEDER; Government of Aragon-FEDER, Grant/Award Number: E35_20R

Abstract

Human riboflavin kinase (*Hs*RFK) catalyzes vitamin B_2 (riboflavin) phosphorylation to flavin mononucleotide (FMN), obligatory step in flavin cofactor synthesis. *Hs*RFK expression is related to protection from oxidative stress, amyloid-β toxicity, and some malignant cancers progression. Its downregulation alters expression profiles of clock-controlled metabolic-genes and destroys flavins protection on stroke treatments, while its activity reduction links to protein-energy malnutrition and thyroid hormones decrease. We explored specific features of the mechanisms underlying the regulation of *Hs*RFK activity, showing that both reaction products regulate it through competitive inhibition. Fast-kinetic studies show that despite *Hs*RFK binds faster and preferably the reaction substrates, the complex holding both products is kinetically most stable. An intricate ligand binding landscape with all combinations of substrates/products competing with the catalytic complex and exhibiting moderate cooperativity is also presented. These data might contribute to better understanding the molecular bases of pathologies coursing with aberrant *Hs*RFK availability, and envisage that interaction with its client-apoproteins might favor FMN release. Finally, *Hs*RFK parameters differ from those of the so far evaluated bacterial counterparts, reinforcing the idea of species-specific mechanisms in RFK catalysis. These observations support *Hs*RFK as potential therapeutic target because of its key functions, while also envisage bacterial RFK modules as potential antimicrobial targets.

KEYWORDS

calorimetry, kinetics limiting step, ligand binding and cooperativity, pre-steady-state kinetics, product inhibition, riboflavin kinase, therapeutic target

Abbreviations: ANP, adenine nucleotide (ATP or ADP); *Ca*, *Corynebacterium ammoniagenes*; CD, circular dichroism; FADS, FAD synthase; FLV, flavinic nucleotide (FMN or FAD); FMNAT, ATP:FMN adenylyltransferase; GST, glutathione S-transferase; HPLC, high-performance liquid chromatography; *Hs*, *Homo sapiens*; ITC, isothermal titration calorimetry; K_a, association constant; k_{cat}, catalytic constant; K_d, dissociation constant; K_i, Inhibition constant; K_M, Michaelis constant; k_{obs}, observed rate constant; k_{off}, dissociation rate constant; k_{on}, association rate constant; PIPES, 1,4-piperazine diethane sulfonic acid; rpm, revolutions per minute; RF, riboflavin, Vitamin B_2; RFK, ATP:riboflavin kinase; SDS-PAGE, sodium dodecyl sulfate-polyacrylamide gel electrophoresis; *Sp*, *Schizosaccharomyces pombe*; *Spn*, *Streptococcus pneumonia*; α, heterotropic interaction constant; ε, extinction coefficient.

1 | INTRODUCTION

Human riboflavin kinase (*Hs*RFK; ECnonbreakingspace2.7.1.26) is an essential enzyme that catalyzes the biosynthesis of the flavin mononucleotide (FMN) cofactor using as substrates riboflavin (RF, vitamin B_2) and ATP, therefore, exhibiting an ATP:riboflavin kinase activity (ECnonbreakingspace2.7.1.26).[1,2] Besides its key role in the synthesis of flavin cofactors, *Hs*RFK is predicted as involved in a protein-protein association network that at the system level affects to different cellular processes (Figure SP1). In this context, the orthologous protein in mice has been shown essential for embryonic development, while, in both human and mouse cells, its binding to the Tumor Necrosis Factor Receptor 1 enhances assembly of the flavin adenine dinucleotide (FAD) cofactor to NADPH oxidases activating the production of reactive oxygen species as defence and signaling molecules.[3] *Hs*RFK expression is also related to cellular protection from progression of some malignant prostate cancers.[4] Recently, RFK, as well as its FMN metabolic product, have also been reported as critical modulators of amyloid-β toxicity.[5] On the contrary, its downregulation alters the expression profiles of cryptochromes and other clock-controlled metabolic genes, being also a potential risk factor for stroke by destroying the protective effect of flavin treatments.[6,7] Finally, insufficient conversion of RF into flavin cofactors by reduction of the RFK activity is reported in protein-energy malnutrition situations coursing with reduced thyroid hormone concentrations.[8-10] Altogether such observations point to *Hs*RFK as a potential therapeutic target.

Part of the FMN produced by *Hs*RFK is directly used as cofactor of FMN-dependent flavoproteins, but most of it is subsequently adenylylated by a FAD synthase (*Hs*FADS), that exhibits ATP:FMN adenylyltransferase activity (FMNAT, ECnonbreakingspace2.7.7.2) and provides the flavin adenine dinucleotide (FAD) cofactor.[11,12] RF to FMN conversion seems to be the major rate limiting step in FAD synthesis, being therefore *Hs*RFK a key element for the production of the FAD cofactor required by more than 60 human flavoenzymes.[13,14] RFK and FMNAT activities located in two independent enzymes is a trait of non-photosynthetic eukaryotes, but in most prokaryotes a single bifunctional enzyme known as type I FAD synthase (FADS) carries out both activities.[15] Noticeably, prokaryotic FADSs fold in two modules, being the N-terminal module associated to the FMNAT activity and the C-terminal to the RFK one.[15,16] The eukaryotic monofunctional RFKs and the C-terminal modules of prokaryotic FADSs are structurally homologs (both folding into a six-stranded β barrel core with Greek key topology), but species-specific differences in secondary structure elements are observed.[1,2,16-18] These variations, although apparently minor, utterly modulate conformational reorganizations occurring during substrate binding and catalysis, as demonstrated for the RFK cycles of the prokaryotic FADSs of *Corynebacterium ammoniagenes* and *Streptococcus pneumoniae* (*Ca*FADS and *Spn*FADS, respectively).[19,20] Furthermore, the substrate binding and catalytic motifs—PTAN and GxY—despite conserved, exhibit species-specific arrangements and traits (Figure1 and SP2).[2,18]

As FMN and FAD are essential cofactors, not only in cell energetics metabolism, but also for the action of a plethora of flavoenzymes with very different cellular functions, their biosynthesis must be thoroughly regulated to maintain cellular and flavoproteome homeostasis.[13,21] In prokaryotes, we recently learned that FMN biosynthesis is regulated through mechanisms that, depending on the species, can include the inhibition of the RFK activity by the RF substrate and/or products, the redox state of the RF substrate, the formation of transient assemblies coupled to catalysis or the subsequent FMNAT activity occurring at the protein N-terminal module.[19,20,22-27] Eukaryotic cells provide additional levels of regulation by making use of different isoforms or intracellular compartmentalization. The mechanisms underlying FMN homeostasis in eukaryotes remain still poorly understood,[28,29] but those found in prokaryotic FADSs might also apply. In this context, the available crystallographic structures of *Hs*RFK and of RFK from the yeast *Schizosaccharomyces pombe* (*Sp*RFK) also envisage large conformational changes upon ligand binding and catalysis, particularly in the surface loops termed FlapI and FlapII (Figure 1 and SP2).[1,2,17]

In the present study, we focus on the intrinsic mechanisms underlying the regulation of *Hs*RFK enzymatic activity. We have used the apo-*Hs*RFK form, to avoid substrates and products of the reaction interfering our experimental approach. Our steady-state data indicate that *Hs*RFK is inhibited by the reaction products, but not by substrates. Stopped-flow spectrophotometry allows ascertaining sequential conformational changes upon ligand binding and catalysis. Finally, ligand binding studies using isothermal titration calorimetry (ITC) display an intricate thermodynamic landscape. Our results are discussed in the context of the here modeled structure for apo-*Hs*RFK, the available crystallographic structures of monofunctional RFKs and previous structure-function studies concerning RFK modules of prokaryotic FADSs.

2 | MATERIALS AND METHODS

2.1 | Cloning, expression, and purification of recombinant *Hs*RFK

The coding sequence of *Hs*RFK (accession number Q969G6) was codon optimized for its heterologous expression in *Escherichia coli* and synthetized by *GenScript*. This DNA sequence was cloned between the *Nco*I and *Bam*HI restriction sites of a pET28a(+)-derived vector, in which the

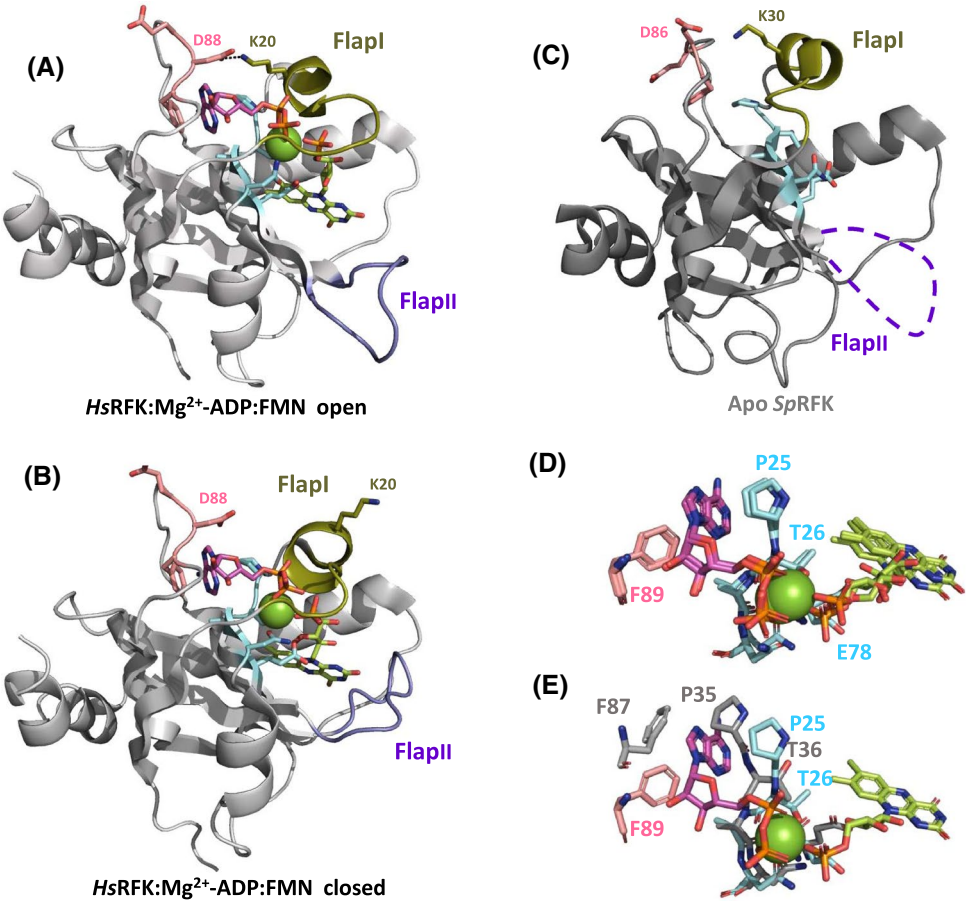

FIGURE 1 Structural properties of RFKs. Cartoon representation of the crystallographic structure of *Hs*RFK in complex with FMN and ADP in either the (A) open (PDB ID 1P4M) or the (B) closed conformation (PDB ID 1Q9S) of the flavin binding site. (C), Cartoon representation of *Sp*RFK as crystallized in the apo form (PDB ID 1N05). FlapII is disordered and depicted as a dashed loop. Comparison of the organization of the active site in the closed *Hs*RFK:FMN:ADP complex relative to the structures of the (D) open *Hs*RFK:FMN:ADP complex and of the (E) apo-*Sp*RFK (shown in grey). In all panels FMN and ADP ligands are shown as CPK colored sticks with carbons in green and magenta, respectively, and Mg^{2+} is shown as a green sphere. Unless otherwise stated, FlapI, FlapII, and L6c are highlighted in green, violet and pink, respectively, the consensus PTAN motif at the active site is in blue for *Hs*RFK and grey for *Sp*RFK. Relevant side-chains are in sticks

thrombin cleavage site was substituted by the PreScission Protease cleavage signal. The sequence-verified plasmid was transformed into *E coli* BL21(DE3) strain, and transformed cells were grown at 37°C in LB medium (1% (w/v) of tryptone, 0.5% (w/v) of yeast extract, and 1% (w/v) of NaCl) supplemented with 50 mg/mL of kanamycin. At an $OD_{600\,nm}$ of 0.7, cultures were induced with 0.2 mM of isopropyl β-D-1-thiogalactopyranoside, incubated under the same conditions and, after 24 hours, harvested. Cells were resuspended in 20 mM sodium phosphate, pH 7.4, 500 mM NaCl, and 10 mM imidazole, containing lysozyme (1 mg/mL), DNase (0.1 mg/mL), and protease inhibitors (0.2 mM of Phenylmethanesulfonyl fluoride and 10 mM of benzamidine), and subsequently sonicated at 4°C. After centrifugation to remove cell debris, the supernatant containing the soluble protein was loaded into a HisTrap HP affinity column (*GE Healthcare*) and the protein was eluted applying a gradient from 10 to 500 mM of imidazole in 20 mM of sodium phosphate, pH 7.4, 500 mM NaCl. Buffer was exchanged to 50 mM Tris/HCl, pH 7.4, 150 mM NaCl, using a HiPrep Desalting Column (*GE Healthcare*). The His_6-Tag was removed by 24 hours incubation with the PreScission protease (*GE Healthcare*) at 4°C, in ratio 1:10 (w/w), and the protein was then loaded into the HisTrap HP column in tandem coupled to a GSTrap 4B column (*GE Healthcare*) to eliminate both the remained His_6-Tagged *Hs*RFK and the PreScission protease (a GST fused product). The resulting yellowish unbound fraction was fractioned with 20% of ammonium sulfate and centrifuged for 30 minutes at 4000 *g*. The supernatant was loaded onto a Phenyl-Sepharose High performance (*GE Healthcare*) column equilibrated with 50 mM of Tris/HCl, pH 8.0, 20% of ammonium sulfate. The column was washed with the same buffer until most of the yellow color washed out. Finally, the protein was eluted using a 20→0% reversed-gradient of ammonium sulfate in the same buffer. Protein purity was

assessed by 17% of SDS-PAGE and buffer was finally exchanged by dialysis in 20 mM PIPES, pH 7.0. Pure protein solution was stored at −80°C until used.

2.2 | Spectroscopic analysis

UV-visible spectra were recorded in a Cary 100 spectrophotometer (*Agilent Technologies*) and ligand-free *Hs*RFK was quantified using the theoretical extinction coefficient $\varepsilon_{279\ nm} = 21\ 430\ M^{-1}cm^{-1}$ and a molecular weight of 17.76 kDa (ProtParam). Fluorescence emission spectra were recorded in a Cary 100 spectrophotometer (*Agilent Technologies*) in 20 mM of PIPES, pH 7.0, 0.3 mM of $MgCl_2$ at 25°C, exciting the protein aromatic residues at 280 nm. Fluorescence excitation scans were recorded at the maximum emission wavelength (323 nm) and in the same experimental conditions. Circular dichroism (CD) spectra were recorded at 25°C using a Chirascan spectropolarimeter (*Applied Photosystem Ltd.*). Samples containing ~5 and ~20 μM of *Hs*RFK in 20 mM of PIPES, pH 7.0, 0.3 mM of $MgCl_2$ were used in the far-UV (cuvette path length, 0.1 cm) and near-UV CD (cuvette path length, 0.4 cm), respectively.

2.3 | Steady-state RFK activity

The RFK activity of *Hs*RFK was measured at 25°C in 500 μL of 20 mM of PIPES, pH 7.0 and 0.3 mM of $MgCl_2$, containing variable concentrations of RF (0.2-15 μM) and ATP (2-600 μM), as previously described.[30,31] The inhibitory effect of the substrates and products of the reaction was also analyzed by measuring the RFK activity in reaction mixtures at increasing concentrations of FMN (0-5 μM), varying the ATP concentration and keeping the RF constant for the determination of the FMN inhibitory effect; and at increasing concentrations of ADP (0-120 μM), varying the RF concentration and keeping ATP fixed. In all cases, reactions were initiated by addition of 40 nM *Hs*RFK to reaction mixtures preincubated at 25°C. After 1 minute of incubation at 25°C reactions were stopped by boiling the samples at 100°C for 5 minutes. The flavin composition of the supernatant was analyzed using an Alliance HPLC system (*Waters*) equipped with a 2707 autosampler and an HSST3 column (4.6 × 50 mm, 3.5 mm; *Waters*) preceded by a pre-column (4.6 × 20 mm, 3.5 mm; *Waters*) as previously described.[31] Flavin concentrations were quantified using RF or FMN standard curves acquired under the same conditions, and the observed steady-state rates for FMN production (v_0) were determined in units of nmoles of flavin transformed *per* min *per* nmol of enzyme (v_0/[*e*]). The kinetic data obtained for one substrate at saturating concentrations of the second substrate were fitted to the Michaelis-Menten kinetic model, obtaining k_{cat} and K_m values. The inhibition mechanism of the products of the RFK reaction -FMN and ADP- was determined by evaluating their effect on K_m and k_{cat} by individual fitting of data sets to the Michaelis-Menten model. Additionally, data sets acquired at variable concentrations of the product acting as inhibitor were globally fitted to the Lineweaver-Burk equation for competitive inhibition

$$\frac{[e]}{v_0} = \left(1 + \frac{[I]}{K_i}\right)\frac{K_m}{k_{cat}}\frac{1}{[S]} + \frac{1}{k_{cat}} \quad (1)$$

where [*S*] is the concentration of the varying substrate (RF or ATP) and [I] that of the inhibitor (FMN or ADP), and K_i is the corresponding inhibition constant. All experiments were performed in triplicate. Estimated errors in k_{cat}, K_M and K_i values were, in general, within 10% of their values, assumed to be larger than the standard deviation between replicates and the numerical error after fitting analysis.

2.4 | Pre-steady-state kinetics

Kinetic experiments in the pre-steady state were registered using stopped-flow spectroscopy on an Applied Photophysics SX17.MV spectrophotometer, using the ProData SX software (*Applied Photophysics Ltd.*) for fluorescence data acquisition and kinetic data analysis. Fast kinetic measurements were carried out at 25°C in PIPES 20 mM, pH 7.0, 0.3 mM of $MgCl_2$ as previously described.[19,20] In short, 0.2 μM of *Hs*RFK was mixed with reaction samples containing increasing concentrations of the FLV ligands in the absence or presence of saturating concentrations of ANP ligands. Evolution of flavin fluorescence after mixing was measured with an excitation wavelength of 445 nm, while fluorescence emission was recovered using a >530 nm cut-off filter. Control experiments, recorded in the same buffer but in absence of $MgCl_2$, produced similar profiles with significantly smaller amplitudes in the fluorescence change. All the concentrations indicated for these experiments are the final ones in the stopped-flow observation cell. Three to five reproducible traces were acquired at each time and concentration condition assayed. These kinetic traces were then fitted to exponential functions,

$$y = \sum A_i \cdot \exp\left(-k_{obsi} \cdot t\right) \quad (2)$$

where A_i and k_{obsi} are the amplitude of the fluorescence change and the observed kinetic constant for a particular spectroscopic process *i* that contributes to the overall time-dependent fluorescence change. The previous equation was corrected by the addition of a linear term when a process was not finished in the timeframe of the measurement.

$$y = \sum A_i \cdot \exp\left(-k_{\text{obsi}} \cdot t\right) + b \cdot t \quad (3)$$

It should be noticed that when more than one process is detected, accuracy in determination A_i and k_{obsi} for processes after the initial one decreases with the FLV concentration assayed.

k_{obs} values showing a linear dependence on the FLV concentration were fitted to a one-step model associated to the binding equilibrium of the flavin ligand to *Hs*RFK (*Hs*RFK+FLV⇆*Hs*RFK:FLV), whose kinetics can be represented by the following equation

$$k_{\text{obs}} = k_{\text{on}} \cdot [\text{FLV}] + k_{\text{off}} \quad (4)$$

where k_{on} and k_{off} are the kinetic rate constants for complex formation and dissociation, respectively.

When k_{obs} values show hyperbolic dependence on the FLV concentration, data can be fitted to an induced fit model (*Hs*RFK+FLV⇆*Hs*RFK:FLV*→*Hs*RFK:FLV)[32] that parametrizes both the ligand binding (K_d, $k_{\text{off}}/k_{\text{on}}$) and the subsequent conformational change (k_r, as the kinetic rate constant for the structural rearrangement).

$$k_{\text{obs}} = k_r \cdot \frac{[\text{FLV}]}{K_d + [\text{FLV}]} \quad (5)$$

When detected, flavin photobleaching within the stopflow observation chamber was evaluated as previously described.[20]

2.5 | Isothermal titration calorimetry

ITC measurements were performed using a high precision Auto-iTC200 MicroCal calorimeter (*Malvern Panalytical*) thermostated at 25°C. Up to 19 injections of 2 μL of the titrating solution were added to the calorimetric sample cell and mixed using a stirring speed of 750 rpm. Ligands and protein were both dissolved in 20mM of PIPES, pH 7.0, in absence and presence of 0.3mM of $MgCl_2$ (cation concentration for optimal enzymatic activity). Typically, 50μM of RF, 70μM of FMN, and 80μM of ANP (ATP or ADP) in PIPES 20mM, pH 7.0 were used to titrate *Hs*RFK (10 μM) in a 200μL sample cell. Additionally, preformed complexes of the enzyme with the FLV or ANP ligands at saturating concentrations were titrated with ANP or FLV ligands, respectively. The association constant (K_a), the enthalpy change (ΔH), and the binding stoichiometry (N) were obtained through nonlinear least squares regression of the data using a homemade model for one binding site, which was implemented in Origin 7.0 (OriginLab) as previously described.[33] The K_d, the free energy change (ΔG), and the entropy change (ΔS) were obtained from essential thermodynamic relationships.

Cooperative ligand binding was assessed by ITC employing an exact analysis of the heterotropic interactions considering a ternary equilibrium between the protein and two ligands approximate analysis as previously described.[34-36] A quasi-binary equilibrium between the protein and one ligand, with the influence of the other ligand being implicit within the apparent ligand binding parameters, was also used to confirm parameters.[20] Briefly, ANP ligands were used to titrate mixtures of *Hs*RFK (10 μM) with different FLV concentrations (0-100 μM) in the calorimetric cell, and the cooperativity constant for the heterotropic interaction (α) between ANP and FLV ligands was determined from any single titration employing the exact methodology.[34-36] Additionally, titrations of *Hs*RFK:FLV mixtures (at different FLV concentrations) with ANP ligands were analyzed as binary titrations, from which apparent association constants for ANP ligands at certain FLV concentrations were determined. These data were fitted to a cooperativity model that considers explicitly the influence of the FLV ligand in the protein binding affinity for the ANP ligand:[19,20,34-36]

$$K_a^{\text{app,ANP}} = K_a^{\text{ANP}} \frac{1 + \alpha K_a^{\text{FLV}} [\text{FLV}]}{1 + K_a^{\text{FLV}} [\text{FLV}]} \quad (6)$$

where $K_a^{\text{app,ANP}}$ is the apparent association constant for the ANP ligand as a function of the FLV concentration, K_a^{ANP} is the intrinsic association constant for ANP (that is, in the absence of FLV ligand), K_a^{FLV} is the association constant for FLV, and [FLV] is the concentration of flavin in the calorimetric cell, from which α between ANP and FLV ligands can also be determined.

ITC experiments were performed in duplicate or triplicate. The errors considered in the measured parameters (in general ±15% in K_d and K_a values, ±0.3 kcal mol^{-1} in ΔH, ΔG and −TΔS, and ±20% in α) were assumed to be larger than the standard deviation between replicates and the numerical error after fitting analysis.

2.6 | Molecular dynamics simulations

The initial model of apo-*Hs*RFK, excluding any ligand, was built by removing ADP and Mg^{2+} from the crystallographic structure with PDB ID 1NB0. PROPKA software was used to assign pK_a values to structures, which were protonated to pH 7.0.[37] PyMOL was used for structural manipulations and figures production.[38] All-atom molecular dynamics (MD) simulations were performed using GROMACS 5.1.5[39] and AMBER ff03 parameters.[40] The system was placed in the center of a rhombic dodecahedron box, solvated with a TIP3P water model and neutralized by adding sodium ions. Final system consisted in 22345 total atoms. A steepest descent minimization was performed to avoid close contacts

or clashes. Desired conditions were achieved after a 100 ps simulation with NVT ensemble and the generation of random initial velocities, and a 100 ps simulation with NPT ensemble, restraining the movement of atoms of protein with a 1000 $kJ \cdot mol^{-1} \cdot nm^{-1}$ harmonic potential. Longer NPT (300 K) simulations with positions unrestrained were then performed, collecting the data every 10 ps. Time step of 2 fs and leap-frog integrator, periodic boundary conditions, Particle Mesh Ewald method for long range electrostatic interaction, Parrinello-Rahman method for pressure control, modified Berendsen method for temperature equilibration and LINCS to restrain bonds including hydrogen atoms were used. Five replicates were made for each trajectory, which were analyzed using VMD[41] and GROMACS package tools.[39]

3 | RESULTS

3.1 | *Hs*RFK is purified free of flavin and adenine ligands

E coli BL21 (DE3) cells transformed with the recombinant pET28a-*Hs*RFK vector produced a high level of expression of active *Hs*RFK enzyme, with a typical yield after purification of 3.2 mg of protein *per* liter of culture. *Hs*RFK fractions were yellow colored, suggesting the protein was expressed in complex with a tightly bound flavinic ligand that kept bound throughout the purification process. Hence, initial purified fractions of the recombinant protein showed the typical flavoprotein bands-I and -II in the Vis absorbance spectrum (Figure SP3A). HPLC analysis of the supernatant obtained upon thermal denaturation of the enzyme demonstrated that the bound cofactor was FMN. Additionally, the other product of the RFK activity, ADP, was also detected as trapped into the purified enzyme. This was evidenced by the displacement of the aromatic absorption peak of protein toward 260 nm (characteristic of nucleotides) in some flavin-free enzyme samples and by the absorption properties of its supernatant after thermal denaturation. High affinity of the adenine nucleotide was previously reported, probably being the reason why all *Hs*RFK structures so far reported in the PDB contain it.[1,2] Therefore, despite the protein was pure, a phenyl-sepharose hydrophobic chromatographic step was required to remove the FMN and ADP products from *Hs*RFK. To the best of our knowledge, this will be the first purification of *Hs*RFK in its apo-form to homogeneity (spectrum shown in Figure SP3A).

Excitation of *Hs*RFK at 280nm produced a fluorescence emission band centered at 332nm (Figure SP3B), in agreement with Trp residues embedded within the protein environment. The negative couplet (195-210 nm) in the far-UV CD spectrum of *Hs*RFK (Figure SP3C) indicated secondary α-helix structure, and the shoulder at 218nm also pointed to an important content of β-sheet. Such spectral properties are consistent with the secondary structure content derived from crystallographic data: around 27% of α-helix, 30% of β-sheet and a large content of loops. The near-UV CD spectrum (Figure SP3D) of *Hs*RFK showed a broad 265-295nm negative band with minima at 285 and 292nm related to the protein tertiary structure organization. Collectively, these data indicate that the purified *Hs*RFK is correctly folded and in the apo-form.

3.2 | The *Hs*RFK activity is modulated by the products of the reaction

In advance to determining the *Hs*RFK kinetic parameters, we quantitatively evaluated the influence of the reducing environment (by using sodium dithionite) as well as of the presence of Mg^{2+}. Under saturating concentrations of both substrates (RF and ATP), the RFK activity resulted tightly regulated by the cation concentration, with maximal rates at a concentration of 0.3mM (Figure SP4A). Herein, a $MgCl_2$ concentration of 0.3mM was used. On the contrary, the rate for RF transformation was independent on the concentration of the reducing agent (Figure SP4B). This later behavior resulted similar to that described for *Ca*FADS and *Spn*FADS, but differed for other species, as *Listeria monocytogenes*, whose turnover and efficiency highly depended on the redox status of the media.[19,22,23,26,27]

Steady-state rates for the *Hs*RFK activity showed saturation profiles for both substrates (Figure 2A). These profiles fitted to the Michaelis-Menten model allowing determination of k_{cat}, K_M^{RF}, and K_M^{ATP}, in 102 min^{-1}, 2.5 μM and 30 μM (Table 1), respectively. Furthermore, no inhibition by excess of RF substrate was detected, contrary to that reported for the RFK activity of *Ca*FADS[31] but in line with previous data for *Hs*RFK,[42] *Spn*FADS,[19] and *Lm*FADS-1.[27] Nonetheless, our *Hs*RFK data showed high efficiency for the synthesis of FMN when compared not only to bifunctional FADSs,[19,20,27] but also to data previously reported for *Hs*RFK[43] (Table 1). In the case of *Hs*RFK, such differences can be associated to different protein isolation procedures, in agreement with early reports showing different RFK pools with distinct enzymatic activity co-existing in rat liver cells. Such differences are probably due to dissimilarities in the content of ligands bound to the enzyme.

Since inhibition of the RFK activity by the reaction products contributes to maintain the flavin and flavoproteome homeostasis in prokaryotes, it is worthy to evaluate the occurrence of such effects in the *Hs*RFK activity. The Michaelis-Menten and Lineweaver-Burk plots at increasing concentrations of either ADP or FMN products showed that while k_{cat} remained constant, both K_M^{ATP} and K_M^{RF} increased (Figure 2). This pointed out to a competitive mechanism of inhibition for both reaction products, allowing determination of the apparent inhibition constants, K_I^{ADP} and K_I^{FMN} (Table 1). The similar values of K_I^{ADP} and K_M^{ATP} as well as of K_I^{FMN} and K_M^{RF} indicated that ADP and FMN bind to the free

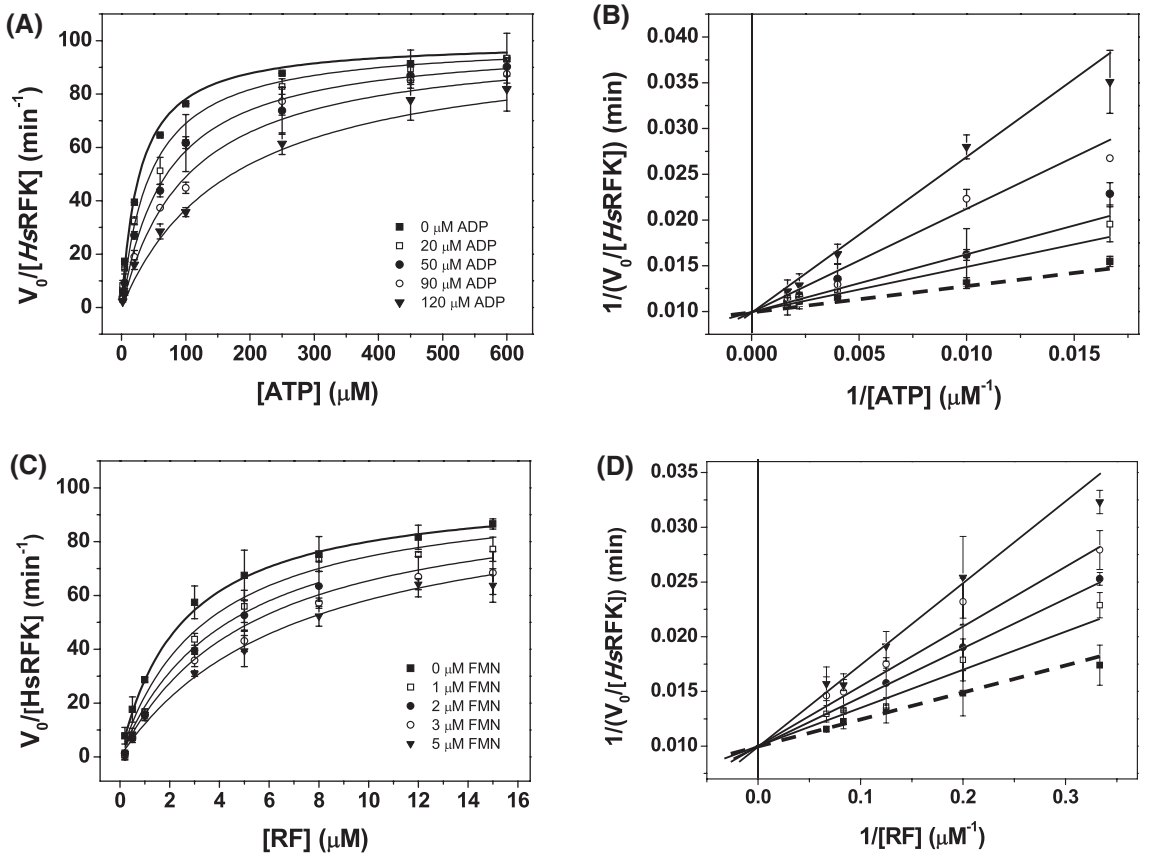

FIGURE 2 Inhibition of *Hs*RFK activity by FMN and ADP products. (A) and (C) Michaelis-Menten plots and, (B and D) their corresponding Lineweaver-Burk representations, as a function of different concentrations of the (A and B) ATP and (C and D) RF substrates in the presence of different concentrations of the products (A and B) ADP and (C and D) FMN. Lines correspond to global fits to the equation for competitive inhibition (Equation 1)

TABLE 1 Steady-state kinetic parameters for the *Hs*RFK activity

RFK enzyme	k_{cat} (min^{-1})	K_M^{ATP} (μM)	k_{cat}/K_M^{ATP} (min^{-1} μM^{-1})	K_I^{ADP} (μM)	K_M^{RF} (μM)	k_{cat}/K_M^{RF} (min^{-1} μM^{-1})	K_I^{FMN} (μM)
*Hs*RFK[a]	102 ± 7	30 ± 8	3.4 ± 1.1	33 ± 6	2.5 ± 0.4	41 ± 9	2.5 ± 0.8
*Hs*RFK(−)[b]	18				117	0.16	
*Hs*RFK(+)[b]	30				36	0.08	
*Ca*FADS[c] RFK module	130 ± 30	40 ± 12	3.2 ± 1.7	17 ± 3	6.9 ± 0.4	19 ± 5	1.4 ± 0.2
*Spn*FADS[d]	55 ± 2	75 ± 7	0.7 ± 0.1	130 ± 16	1.2 ± 0.3	46 ± 13	1.3 ± 0.4
*Lm*FADS-1(−)[e]	33 ± 2	41 ± 2	0.8 ± 0.1	844 ± 95	0.5 ± 0.1	66 ± 4	7.1 ± 1.3
*Lm*FADS-1(+)[e]	95 ± 7	12 ± 1	7.9 ± 0.9		10 ± 1	95 ± 1	

[a]Experiments performed at 25°C in 20mM of PIPES, pH 7.0, 0.3 mM of $MgCl_2$ (n = 3, mean ± SD). Presented data calculated by global fitting.

[b]Data from (43). Experiments performed at 37°C in 50 mM of potassium phosphate buffer, pH 7.5, 12mM of $MgCl_2$, both in absence (−) and presence (+) of 24 mM of sodium dithionite.

[c]Data from (20). Experiments performed at 25°C in 20mM of PIPES, pH 7.0, 0.8 mM of $MgCl_2$.

[d]Data from (19). Since both ADP and FMN act as mixed inhibitors two different K_I values are shown for each. Experiments performed at 25°C in 20 mM of PIPES, pH 7.0, 0.8 mM of $MgCl_2$.

[e]Data from (27), experiments performed in 20mM of PIPES and 0.8 mM of $MgCl_2$, pH 7.0, at 25°C, both in absence (−) and presence (+) of 24 mM of sodium dithionite.

*Hs*RFK enzyme with alike affinity to the substrates of the reaction. Also, the significantly smaller inhibition constant for FMN in comparison with ADP (K_I^{ADP}/K_I^{FMN} = 13.2) envisages FMN as a more potent inhibitor.

*Ca*FADS and *Spn*FADS also showed product inhibition of the RFK activity, but their inhibition mechanisms differed from that of *Hs*RFK as well as among them: mixed for both products in *Spn*FADS *versus* competitive for FMN and

uncompetitive for ADP in *Ca*FADS. FMN is a more potent inhibitor in *Ca*FADS ($K_M^{RF}/K_I^{FMN} = 7.1$) than in *Spn*FADS or *Hs*RFK (0.8 and 1, respectively); and also, RF is a very strong inhibitor of the RFK activity in *Ca*FADS but not in the other enzymes.[19,20,27] Therefore, FMN biosynthesis in *Homo sapiens* will be regulated by the products of the RFK reaction. In addition, and considering that transport across membranes appears favored for the RF substrate over FMN and FAD, intracellular compartmentalization with different substrate/product concentrations and/or the presence of different isoforms might also apply in the *in vivo Hs*RFK regulation.[11,28,44]

3.3 | Binding of *Hs*RFK substrates is the kinetically preferred process

We used stopped-flow spectrophotometry to kinetically differentiate individual processes during the *Hs*RFK reaction. This technique allowed us to detect small changes in the dielectric environment of the flavin isoalloxazine upon its binding and/or dissociation to the protein, and/or as consequence of conformational changes in its environment,[19,20] while RF transformation into FMN is not observed due to the same fluorescence spectra and quantum yields of both flavins. When we mixed *Hs*RFK with either RF or FMN, we only detected very slow and linear fluorescence decays consistent with previously reported flavin photobleaching.[19,20] These observations suggested that the apo-form of *Hs*RFK is not able to bind RF or FMN (herein both referred as FLV) ligand, or at least to internalize its isoalloxazine ring in the expected catalytically competent enclosed conformation.

A fast and intense exponential decay in fluorescence in the 2 seconds time frame was, however, detected when mixing *Hs*RFK with all combinations of ATP or ADP (denoted herein as ANP) and FLV ligands (Figure 3A). We related the fluorescence decay to FLV binding and/or internalization in the protein matrix by FlapII displacement (Figure 3A), concluding that the ANP presence/binding prones *Hs*RFK to bind and internalize the FLV ligand. Noticeably, no subsequent recover of fluorescence was observed for the assayed

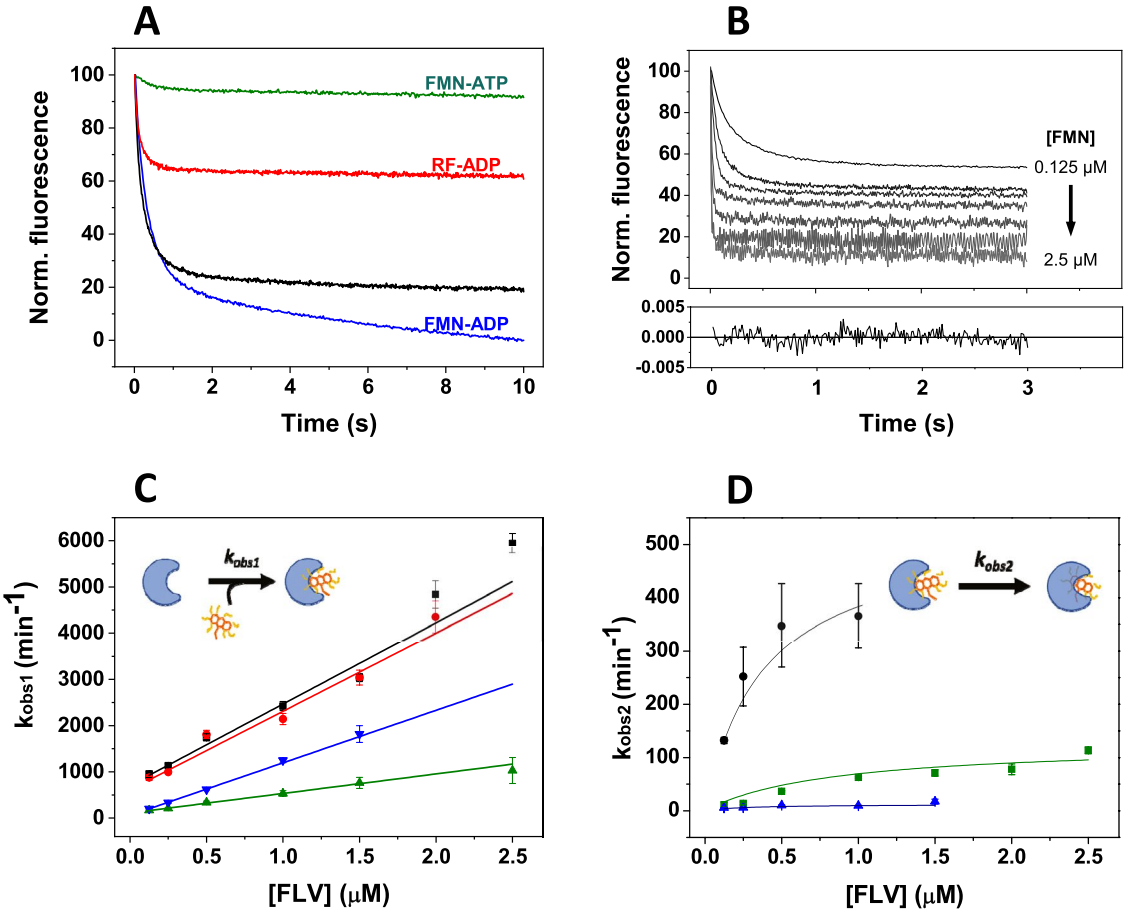

FIGURE 3 Pre-steady-state stopped-flow kinetics of the binding of RF and FMN to *Hs*RFK in the presence of adenine nucleotides. (A) Normalized evolution of kinetic changes in fluorescence upon mixing *Hs*RFK (0.2 μM) with all possible FLV-ANP ligand combinations (0.125 and 250 μM, respectively). (B) Example of the fittings of kinetic traces (in this case, corresponding to mixtures of *Hs*RFK with RF-ATP), and residuals of the fitting of the 1 μM RF-250 μM ATP data to a biexponential function. Evolution of (C) k_{obs1} and (D) k_{obs2} as a function of the FLV concentrations. Insets show schemes representing the corresponding processes

combinations of ligands, differing this behavior from the one reported when similarly evaluating the RFK modules of *Ca*FADS and *Spn*FADS. For these two enzymes, the initial flavin fluorescence decay was followed by fluorescence recover related to an ATP-induced conformational change that re-opens the flavin binding site making the isoalloxazine accessible to the solvent after the reaction has taken place.[19,20]

Kinetic traces corresponding to mixtures of *Hs*RFK with the RF-ADP ligands fitted to a single exponential decay, whereas two and up to three independent processes were identified when, respectively, evaluating the binding kinetics in the FLV-ATP and FMN-ADP combinations (Figure 3B). Noticeably, while the amplitude of the first process (A_1) dominates the fluorescence decay for RF binding, A_1 and A_2 became similar when assaying the binding kinetics of the FMN product (no shown). Therefore, we identified the initial process, generally accounting for most of the amplitude decay, as FLV binding/internalization in *Hs*RFK by FlapII displacement (up to ~14Å reorganization of amino acids comprising the loop), similarly to that reported for *Ca*FADS and *Spn*FADS.[19,20] The succeeding fluorescence decays have to relate to subsequent conformational changes in *Hs*RFK loops further contributing to additional changes in the isoalloxazine environment after the initial binding. Considering these extra processes are not observed when mixing the protein with RF-ADP, they appear related to the extra phosphates of ATP and FMN, over ADP and RF, respectively, influencing some conformational flexibility.

k_{obs1} values showed a linear dependence on the FLV concentration (Figure 3C) that permitted to determine k_{on} and k_{off} for flavin binding and, as a consequence the process dissociation constant (K_d) (Table 2). These data indicated that binding processes containing the RF substrate are the fastest (Table 2A). In addition, the largest amplitude in fluorescence decay is observed for RF and ATP (Figure 3A). Therefore, *Hs*RFK binds preferably the substrates of the RFK reaction, RF and ATP, over other combinations of substrates/products, similarly to *Spn*FADS but contrary to *Ca*FADS. Noticeably, binding of the FMN product in presence of ANP (particularly ATP) were the least favored processes from the kinetic point of view (smaller k_{on}), though the combination of FMN-ADP products showed an amplitude comparable to that of substrates and a considerably lower k_{off}. As consequence, the complex of *Hs*RFK with the products of its activity exhibits the smaller K_d and appears, therefore, as the most stable one.

On their side, when detected, k_{obs2} showed a saturation profile on the FLV concentration (Figure 3D). When fitting these data to an induced fit model representing changes in the protein conformation induced by binding of the ligand,[32] we were able to determine an equilibrium reorganization constant as well as the kinetic constant to achieve the final state (Table 2B). Noticeably, this process presented very particular features when evaluating the FMN-ADP products; it was considerably slower (k_r), A_2 was comparable to A_1, and the product of its reorganization was the most stable (K_{reorg}). Therefore, binding of the products of the RFK activity to the enzyme occurs through stabilization of a transient intermediate in the isoalloxazine internationalization by FlapII displacement, while these intermediate is hardly populated, or not at all, in the binding of other ligand combinations. Noticeably, this FMN-ADP combination is the only one for which a third considerably slower process (80-100 min^{-1} at the FMN concentrations assayed), likely independent of the flavin concentration, is observed when binding to *Hs*RFK. Interestingly, k_{on} and k_r values for the binding of RF-ATP substrates are substantially faster than the k_{cat}, while k_{off} for the FMN-ADP products is situated in its range (Tables 1 and 2). Collectively, these observations indicate that kinetics of products release limits the *Hs*RFK catalytic activity.

These data point to differences in the regulation of the catalytic activity of *Hs*RFK when compared to *Ca*FADS and *Spn*FADS. In *Hs*RFK, as in *Spn*FADS, the binding of substrates of the RFK reaction -RF and ATP- is the kinetically favored process,[19] whereas in *Ca*FADS binding of any other combination of ligands is faster.[20] Moreover, while in *Ca*FADS and *Spn*FADS the ATP substrate activates FLV ligand internalization as well as the subsequent cavity reopening to make this ligand again solvent accessible, such

TABLE 2 Pre-steady-state kinetic parameters for the binding and dissociation of flavins to *Hs*RFK in the presence of adenine nucleotides. Experiments were performed at 25°C in 20 mM of PIPES, pH 7.0, 0.3 mM of $MgCl_2$ (n = 5, mean ± SEM) in and stopped-flow equipment

	k_{obs1} (flavin binding)				k_{obs2} (conformational rearrangement)		
Ligands combination	k_{on} (min^{-1} μM^{-1})	k_{off} (min^{-1})	K_d (μM)	ΔG (kcal mol^{-1})	k_r (min^{-1})	K_{reorg} (μM)	ΔG_{reorg} (kcal mol^{-1})
RF-ATP	1760 ± 50	700 ± 40	0.40 ± 0.02	−8.6 ± 0.1	530 ± 80	0.38 ± 0.08	−8.8 ± 0.1
RF-ADP	1670 ± 90	610 ± 10	0.36 ± 0.03	−8.7 ± 0.1	–[a]	–[a]	–[a]
FMN-ATP	420 ± 40	110 ± 10	0.26 ± 0.04	−8.9 ± 0.1	127 ± 14	0.83 ± 0.41	−8.3 ± 0.3
FMN-ADP	1140 ± 30	59 ± 8	0.05 ± 0.01	−9.9 ± 0.1	12 ± 2	0.16 ± 0.1	−9.2 ± 0.4

[a]Process not observed for this combination of ligands.

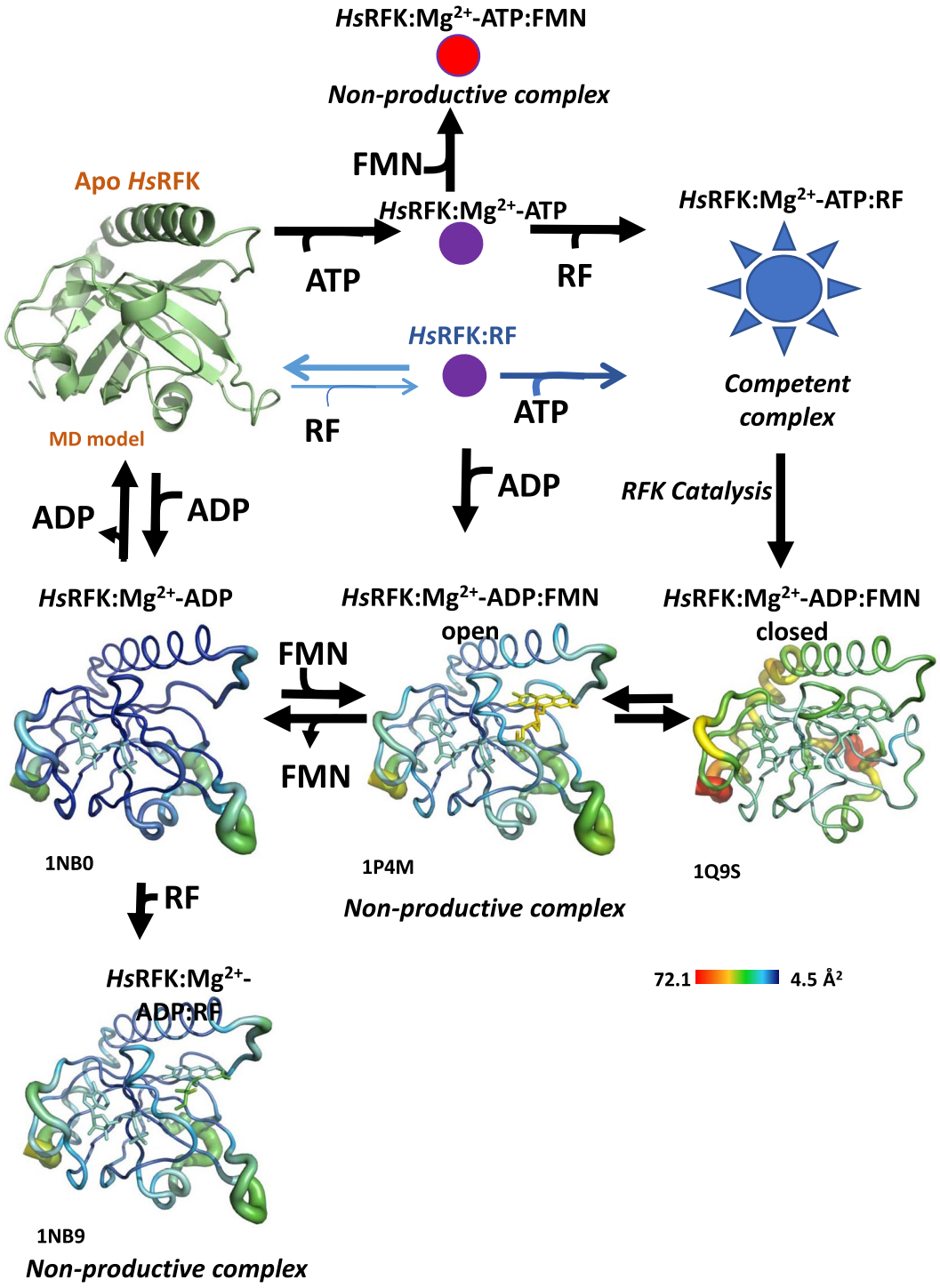

FIGURE 4 Scheme of the conformational and ligand binding spaces along the *Hs*RFK cycle. The diagram summarizes the different *Hs*RFK species envisaged considering kinetic, inhibition, binding, and structural data available. All presented structures correspond to different crystal structures for *Hs*RFK (PDB IDs are indicated), with the only exception of the apo-form that has been produced by MD simulations of the 1NB0 pdb after removing the ADP:Mg^{2+} ligand. Crystal structures are represented by B-factor of backbone atoms, with higher radius of ribbons and warmer colors indicating higher fluctuations, being all snapshots normalized according the color code. Those states lacking structural data are represented by circles (nonproductive states are shown in red, alternative paths in violet and competent state in blue start). Processes leading to the formation of sub-stoichiometric complexes (*Hs*RFK:RF) are highlighted with blue arrows

final exposure is not detected with *Hs*RFK. In addition, this enzyme is the only from the three for which k_{off} for the FMN-ADP ligands is considerably slower than k_{on} (nearly 20-fold), making the binding of the products stronger and envisaging different mechanisms for the FMN product release from the RFK site among these three proteins.

3.4 | Thermodynamics modulates the ligand binding landscape of *Hs*RFK

Subsequently, we performed ITC experiments to assess if the kinetically detected processes were significant in reaching the thermodynamic equilibrium. Binary and ternary interactions of *Hs*RFK with ANP and/or FLV ligands were analyzed at pH 7.0 and 25°C both in absence and in presence of 0.3 mM of Mg^{2+}. The corresponding determined thermodynamic parameters are summarized in Table SP1, while some examples of the experimental thermodynamic dissections are displayed in Figure SP5.

Direct titrations allowed the determination of the intrinsic binding parameters of the interaction of *Hs*RFK with substrates and products of the RFK reaction. For ANP ligands, K_d^{ANP} values were in the low micromolar range and the stoichiometry of the interaction, around 0.6, was consistent with a unique ANP-binding site, with occupancy below unity being probably associated to protein conformational heterogeneity. This agrees with low B-factors of the bound ADP-Mg^{2+} in the available crystallographic structures (Figure 4). The presence of Mg^{2+} resulted in the reduction of the favorable enthalpic contribution to binding, as well as of the unfavorable entropic one (Figure SP6). Nonetheless, ΔG remained mostly insensitive to the cation through entropy/enthalpy compensation. A similar situation was previously reported for the RFK module of *Ca*FADS.[33] On the contrary, FLV (RF and FMN) ligands were hardly able to directly bind *Hs*RFK. No interaction heat was detected for the protein titration with FMN, suggesting either lack of interaction, very slow binding or interaction occurring without appreciable exchange of heat. In titrations with the RF substrate, data allowed for estimation of a K_d^{RF} value in the micromolar range, but the low interaction stoichiometry observed envisages very low occupancy (N around 0.16). Mg^{2+} further hindered RF binding due to a higher increase in the entropic contribution to the binding than in the enthalpic one (2.32- and 1.37-fold, respectively) (Table SP2, Figure SP6).

Titrations of ANP:*Hs*RFK or FLV:*Hs*RFK binary mixtures with, respectively, FLV or ANP permitted to further unravel the complete thermodynamic landscape of ligand binding. Figure 5 summarizes all possible binary and tertiary interactions of the enzyme with substrates and products in absence (Figure 5A) and presence of Mg^{2+} (Figure 5B), including the fraction of binding-competent protein (N) in each case as the thickness of the arrows. Titrations involving both RF and ATP in the presence of the divalent cation (catalytic conditions) were not measured, since the heat of the catalytic reaction masked the interaction heat. As shown in the figure, pathways leading to non-competent tertiary complexes compete with formation of the *Hs*RFK:ATP:RF catalytically complex (orange pathways in Figure 5). Nevertheless, there was no thermodynamically preferred binding pathway, both in terms of final complex stability and production probability (N, interaction stoichiometry). The presence of Mg^{2+} slightly increased the fraction of protein prone to interact and, consequently, the probability of a particular path to occur, but, contrary to *Ca*FADS and *Spn*FADS,[19,20] hardly modulated the binding landscape (Figure 5A,B, SP5, Table SP1). The only exception to this behavior was observed for the FMN-ADP products combination, where the cation presence made enthalpic as well as entropic contributions to the *Hs*RFK binding favorable. Therefore, differences in conformation of ternary *Hs*RFK complexes as a consequence of the cation

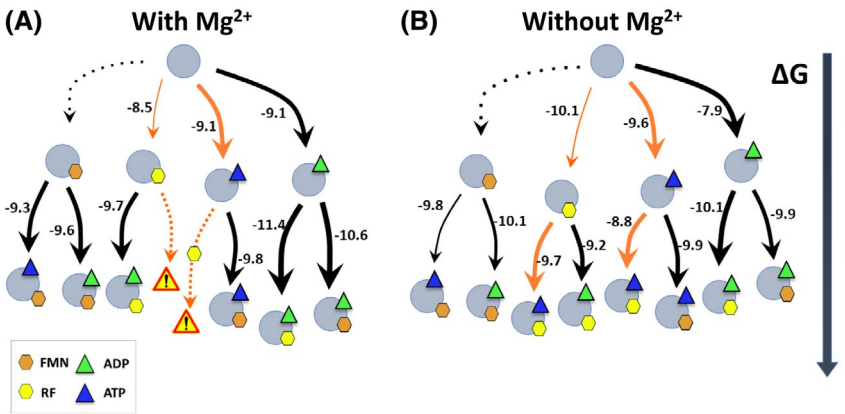

FIGURE 5 Gibbs free energy flow for the interaction of *Hs*RFK with substrates and products. Diagrams summarize the thermodynamics of the interaction of *Hs*RFK with different combination of its ligands as obtained by ITC (Table SP1) at 25°C (A) in 20 mM of PIPES, pH 7.0, 0.3 mM of $MgCl_2$, and (B) in 20 mM of PIPES, pH 7.0. *Hs*RFK is represented as blue spheres, RF and FMN as orange and yellow hexagons, and ATP and ADP as green and blue triangles, respectively. The length of the arrows is proportional to the ΔG for the interaction (value in kcal mol^{-1} are indicated in numbers), and its thickness is representative to the fraction of *Hs*RFK binding the titrating ligand. Processes not directly observed by ITC (interaction of *Hs*RFK with FMN) are shown as dotted arrows. Paths leading to the formation of the tertiary catalytic complex (*Hs*RFK with ATP and RF substrates) are highlighted with orange arrows. NM indicates processes that could not be measured in the presence of Mg^{2+} since the reaction heat would mask the interaction heat

TABLE 3 Cooperativity coefficients for the binding of the different combinations of FLV and ANP ligands to *Hs*RFK in presence and absence of Mg^{2+}. Experiments were performed at 25°C in 20mM of PIPES, pH 7.0, both in absence and presence of 0.3mM of $MgCl_2$. (n = 5, mean ± SEM)

[$MgCl_2$]	Ligands	α	N	Δh kcal/mol
0.3 mM	RF-ATP	N.M.[a]	N.M.[a]	N.M.[a]
	RF-ADP	2.2 ± 0.2	0.62 ± 0.01	−1.3 ± 0.2
	FMN-ATP	1.4 ± 0.1	0.49 ± 0.01	6.2 ± 1.0
	FMN-ADP	2.0 ± 0.2	0.50 ± 0.01	−10 ± 0.3
0 mM	RF-ATP	0.87 ± 0.20	0.68 ± 0.01	5.3 ± 0.4
	RF-ADP	8.3 ± 1.2	0.46 ± 0.01	1.8 ± 0.6
	FMN-ATP	0.96 ± 0.10	0.61 ± 0.01	2.7 ± 0.2
	FMN-ADP	6.9 ± 1.2	0.56 ± 0.01	−5.9 ± 0.6

[a]N.M., not measured. When mixing RF and ATP in presence of Mg^{2+}, the catalytic reaction heat conceals the interaction heat.

presence are only predicted for the formation of the ternary complex containing the FMN and ADP products, contrary to that reported for *Ca*FADS and *Spn*FADS.[19,20] The energy diagram in the absence of $MgCl_2$ (Figure 5B) showed two alternative pathways leading to *Hs*RFK:ATP:RF "pseudo-reactive" complexes, which in addition are among the most probable. Therefore, the *Hs*RFK behavior is more similar to *Spn*FADS than to *Ca*FADS, enzyme that favors all the other nonproductive *Ca*FADS:ANP:FLV complexes against the *Ca*FADS:ATP:RF one.[19,20]

3.5 | ANP and FLV ligands cooperate in their binding to *Hs*RFK

Although direct FLV binding to the free protein was hardly observed by ITC or stopped-flow spectrophotometry, the presence of FLV increased *Hs*RFK affinity for ANP ligands, particularly when the cation is present (compare ΔG values for the titrations of free *Hs*RFK and binary mixtures, Table SP1, Figure 5A and SP6). These observations suggest that, as in the bacterial RFK modules, (a) FLV ligands have a slow-binding mode to *Hs*RFK that permits to indirectly estimate their binding parameters [34,45,46] and (b) ANP and FLV show cooperativity in their binding.

To evaluate cooperativity, we titrated *Hs*RFK:FLV binary mixtures with ANP and fitted the resulting thermograms to a model for heterotrophic interactions applying, as explained in Materials and Methods section, two complementary methodologies.[34,36,46] Our data, summarized in Table 3, show that Mg^{2+} modulates ligand binding cooperativity to *Hs*RFK. In its presence, FLV and ANP ligands show positive cooperativity ($\alpha > 1$). When Mg^{2+} is absent, RF-ADP and FMN-ADP binding cooperativity increases (up to 4-fold and 3-fold, respectively), while binding cooperativity becomes slightly negative for the RF-ATP substrates combination ($\alpha < 1$). In general, the magnitudes of the cooperativity constants for ligand binding to *Hs*RFK are moderated and in the range of those for *Spn*FADS, while those for *Ca*FADS are considerably larger, particularly in the presence of $MgCl_2$. Cooperativity in RF and ATP substrates binding to *Hs*RFK and *Spn*FADS is slightly negative and positive, respectively. Noticeably, in the case of *Ca*FADS its sign and magnitude are highly influenced by the RF substrate concentration that in this case also acts as inhibitor.[19,20] Thus, differences are also found in the cooperation of substrates and products binding to RFK enzymes from different organisms.

4 | DISCUSSION

4.1 | Conformational landscape in the *Hs*RFK catalytic cycle

To date, there is no an available 3D crystal structure of *Hs*RFK in the absence of any ligand, either ANP or FLV, or both. To gain insight into such conformation, we generated a model of apo-*Hs*RFK by removing Mg^{2+}:ADP from the *Hs*RFK-Mg^{2+}:ADP crystal structure (PDB ID 1NB0). This model was minimized and relaxed by MD simulations (5 replicas) (Figure6 and SP7). Trajectories for Cα root mean square deviation (RMSD), energy, solvent accessible surface (SAS) and radius of gyration (GyR) indicate that apo-*Hs*RFK keeps overall folding along simulations (Figure SP7). The most remarkable fact was the transient breaking of the Lys20-Asp88 salt bridge, with the consequent displacement of FlapI and loop 5 (L5c), and the observation of a dynamic opening/closing of the ADP/ATP-binding cavity (Figure 6). On the contrary, the conformation of the active site, formed by the consensus PTAN motif and Glu78, retained conformations similar to those observed in the crystal binary- and ternary- *Hs*RFK complexes (Figure 6C and SP8). Such conformations resemble those in the apo-forms of *Sp*RFK and RFK module of *Spn*FADS (Figure 1 and SP7). This leaves apo-*Ca*FADS as the only RFK showing a different PTAN conformation due to its Thr exhibiting considerably different Φ and ψ values (Figure SP8A). In conclusion, our MD data show that FlapI and L5c adopt different conformations in apo-*Hs*RFK with respect to binary *Hs*RFK:ADP complexes.[2] Additionally, our simulations predict an open Flavin binding site for apo-*Hs*RFK, while crystal structures indicate that closed conformations must be populated in ternary complexes due FlapII displacement toward this cavity (Figure 1 and SP2).[17] Therefore, it is accepted that *Hs*RFK must undergo a series of sequential conformational changes during the catalytic cycle (Figure 4).

An ordered bi-bi mechanism for mammalian RFKs was previously proposed, in which RF binding was followed by

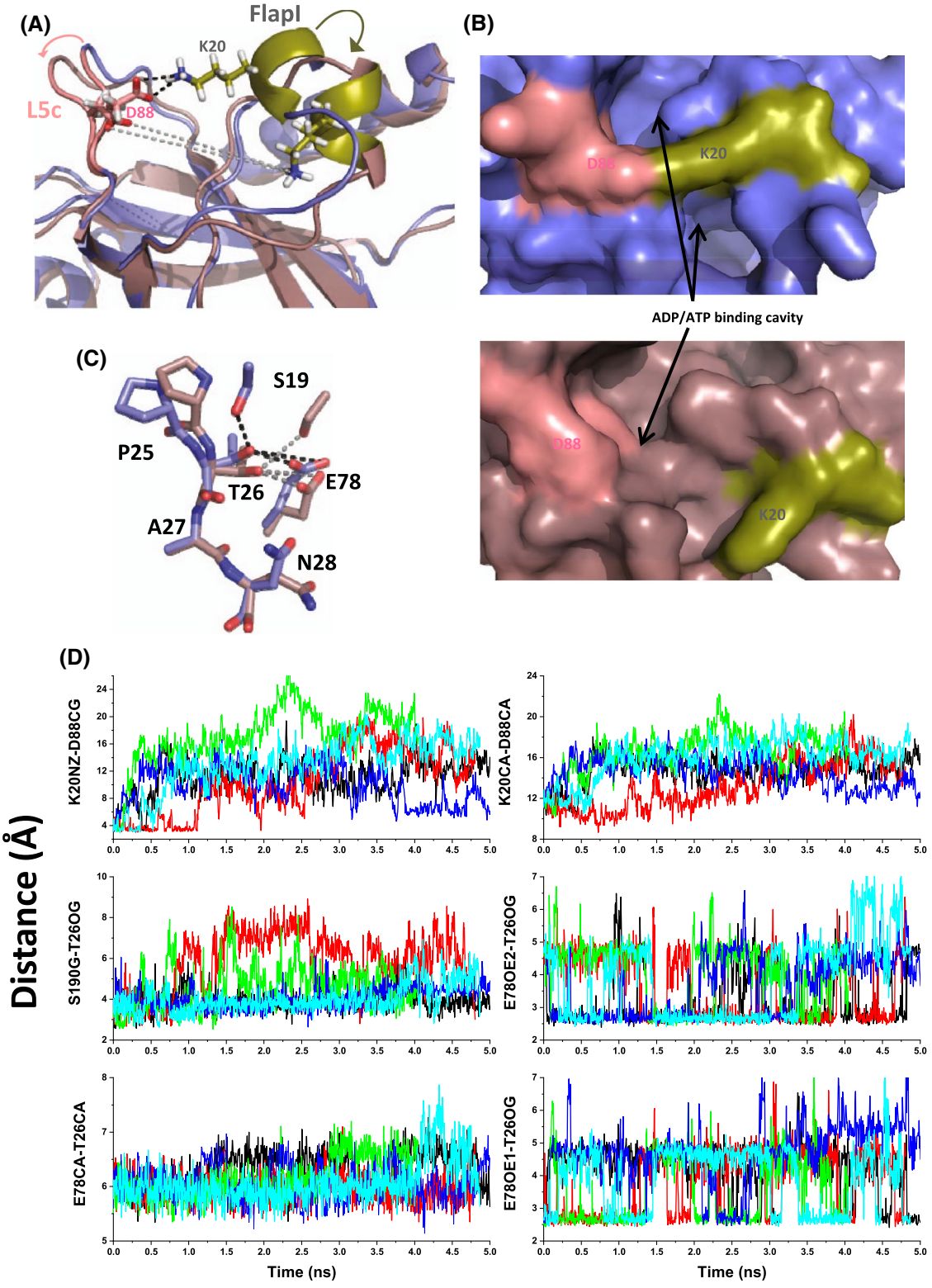

FIGURE 6 The apo-*Hs*RFK structural model. (A) Cartoon overlapping and (B) surfaces around the ADP/ATP binding site of apo-*Hs*RFK structural models for the starting structure (violet) and the snapshot after 5 ns of MD (brown). L5c and FlapI are, respectively, colored in salmon and olive. Side chains for Lys20 and Asp88 are shown in sticks. (C) Stick representation of the conformation of the PTAN motif and the catalytic residue Glu78 in the starting structure (violet) and the snapshot after 5 ns of MD (brown). Panels A-C show snapshots of replica 1, and initial distances among selected atoms are shown as black dashed black lines, while corresponding distances at the end of the simulation are shown as grey dashed lines. (D) Trajectories for the evolution of the relative distances between residues Lys20 and Asp88, as well as among Thr26 at the PTAN motif and Ser19 and Glu78 along 5ns MD simulations of apo-*Hs*RFK. Data are shown for the 5 replicates. Simulations carried out at 300 K

ATP binding, being ADP and FMN subsequently released after catalysis.[1,2,47] However, our ITC and stopped-flow experiments demonstrate that FLV (RF and FMN) ligands hardly interact with *Hs*RFK in the absence of ANP ligands. The interaction of RF detected by ITC—a minority pathway in the whole interaction landscape—might be associated to the slow binding of a few molecules, probably associated to RF molecules recognizing some motives of the large flavin binding site in the open conformation expected in apo-*Hs*RFK (Figure 4) (as observed in *Sp*RFK[17]). Nonetheless, RF recognition in this state appears scarce, slow and unable to trigger by itself the structural reorganization of FlapII. This is confirmed by the absence of changes indicative of internalization of the isoalloxazine ring in our stopped-flow experiments as well as in the crystallographic structures (differences in FlapI and FlapII disposition relative to *Hs*RFK:ADP:FMN complex, Figures 1, 4 and SP2). Nonetheless, the larger magnitudes for the entropic and enthalpic contributions for ATP binding to apo-*Hs*RFK when compared to the *Hs*RFK-RF mixture (Table SP1 and Figure SP6) point to structural rearrangements associated to the RF presence in its binding cavity that favors ANP binding. Nonetheless, even if RF favors the initial binding of ANP, the accommodation of the ANP in the cavity and the establishment of new FlapI-ANP interactions probably elapses the initial nonproductive RF interaction mode to a new one. Thus, conformational changes in FlapI have also an effect in FlapII conformation (see FlapI and FlapII in *Hs*RFK:ADP:FMN crystal structures, Figure 1 and SP2), further contributing to place RF in an arrangement compatible with catalysis.[1,2] Our transient kinetic experiments support such mechanism, since FlapII displacements can be indirectly perceived by the changes in flavin fluorescence. Thus, for mixtures of *Hs*RFK with FMN-ANP, we observed a slower reorganization process consistent with additional isoalloxazine burial into the binding pocket by FlapII reorganization. However, in the case of RF-ATP mixes, k_2 is relatively faster and shows lower amplitude, probably only reflecting the protein dynamics during the catalytic turnover. Noticeably, our stopped-flow data also envisage that after catalysis the flavin binding site of *Hs*RFK remains blocked by FlapII (Figure 4), making FMN release the rate-limiting step in FMN production and envisaging that this reaction process might be controlled by factors different from the protein itself. In this context, it is worth to note that *Hs*FADS, besides its FMNAT activity, also operates as a FAD chaperone for flavin delivery to its client apoproteins.[29,48] Our data envisage that a similar mechanism might apply in *Hs*RFK for FMN transfer to *Hs*FADS as well as to FMN dependent client apoproteins, with direct protein-protein interaction favoring FMN release from *Hs*RFK. Such tight regulation agrees with FMN, as well as FAD, being crucial cofactors in a pletora of enzymes devoted to manage cell bioenergetics.

4.2 | Different organisms, different regulatory strategies

Our previous hypothesis of a species-specific inhibition and activity modulation of the RFK activity in bifunctional FADS is here reinforced, as well as extended to monofunctional proteins, by the *Hs*RFK data. Despite the overall structural similarity among eukaryotic RFK enzymes and prokaryotic RFK-modules (RMSD of core Cα positions are only 1.2, 1.6, and 1 Å when comparing *Hs*RFK with *Sp*RFK, *Ca*FADS, and *Spn*FADS, respectively), differences among species occur in the conformation of several structural elements, including the FlapI and FlapII loops, and, particularly, the catalytic PTAN motif (Figure SP8A).[18] In this structural context, activity and binding studies reflect some common regulatory mechanisms, as well as highly relevant differences among *Hs*RFK and the RFK-modules of *Ca*FADS and *Spn*FADS. These variations modulate ligand binding and, consequently, catalytic cycles, resulting in a variety of species-specific mechanisms regulating the biosynthesis of flavin cofactors.

Thus, the inhibition of the RFK activity by the products of the reaction seems to be common for all of them, although inhibition potency and mechanism varies with the enzyme. For example, *Ca*FADS is more strongly inhibited by both reaction products as deduced from the K_I^{FMN}/K_M^{RF} and K_I^{ADP}/K_M^{ATP} ratios (0.2 vs 1 and 1, and 0.42 vs 1.16 and 11.2, for *Hs*RFK and *Spn*FADS, respectively).[19,20] Kinetic data for binding are consistent with these differences, since binding of the RFK reaction products is kinetically preferred in *Ca*FADS, while *Hs*RFK and *Spn*FADS bind the substrates faster. Thermodynamics also shows that pathways leading to the catalytic RFK complex are un-favored respect to those leading to "pseudo-reactive" complexes in *Ca*FADS,[20] whereas these differences either do not exist or favor formation of the catalytic complex in *Hs*RFK and *Spn*FADS, respectively (Table SP1).[19] Differences are also observed in heterotropic ligand binding cooperativity. Cooperativity seems to be determinant in regulating RFK activity in *Ca*FADS, while in general the *Hs*RFK behavior is more modest and resembles that of *Spn*FADS. Thus, our data indicate that *Hs*RFK, *Ca*FADS, and *Spn*FADS achieve the catalytic RFK:RF:ATP complex through mechanisms exhibiting relevant differences. *Hs*RFK and *Spn*FADS follow a random sequential binding of the RFK substrates, while substrates binding to *Ca*FADS is concerted. Differences in the substrates cooperative behavior and magnitude might relate also to the different conformations of the PTAN motif among species (Figure SP8A), which points to specific conformational changes during the RFK activity. In *Ca*FADS, the occupation of the ANP binding site by RF—when it is in excess—might prevent the ligand-induced conformational change of this motif, which is necessary for ATP binding.[18] This structural rearrangement is not expected to be necessary neither for *Hs*RFK (Figure 1D,E) nor for *Spn*FADS.[19] Therefore, the absence of

inhibition by RF in *Hs*RFK and *Spn*FADS might be associated to the minimal rearrangement of PTAN motif during the catalytic cycle of these enzymes.

For all three proteins release of FMN and ADP products appears to be the reaction limiting step, but clear differences are also envisaged in the conformation of such ternary complex in solution. Thus, our stopped-flow analyses suggest that FMN is not accessible to the solvent when the *Hs*RFK:FMN:ADP complex is in solution, while it is accessible when similarly evaluating the RFK modules of *Ca*FADS and *Spn*FADS. This might implicate different modes for the transfer of the newly synthesized FMN to the client proteins. In this context, we must also consider that while eukaryotic RFKs are relatively small, monofunctional and monomeric proteins, their bacterial counterparts have an additional FMNAT module that duplicates its size.[16] Moreover, these bifunctional enzymes can stabilize quaternary assemblies with direct interaction of RFK and FMNAT ligand binding cavities, which potentially will contribute to FMN release from the RFK module by direct transfer to the FMNAT module as well as to regulate FlapII conformation and flavin accessibility to the solvent.[16,25]

In conclusion, we present here an integrated thermodynamic and kinetic description of the catalytic mechanism of *Hs*RFK that might contribute to the better understanding of the molecular bases of certain pathologies coursing with changes in the expression or catalytic efficiency of this protein. We also report key thermodynamic, kinetic and structural differences of the regulation of the *Hs*RFK catalytic cycles relative to bacterial modules performing the same activity. To date, antimicrobials only targeting the FMNAT activity of prokaryotic FADSs have been investigated,[49] probably because of the overall sequence and structural similarity of their RFK module to their eukaryotic counterparts envisaged specificity compromise and as a consequence deleterious effects to the host.[50] However, the here presented data also foresee that the bacterial RFK activity might be consider a potential antimicrobial target for some bacterial pathogens.

ACKNOWLEDGMENTS

Authors would like to acknowledge the use of Servicios Generales de Apoyo a la Investigación-SAI, Universidad de Zaragoza.

CONFLICT OF INTEREST

The authors declare no conflict of interest. The funders had no role in the design of the study; in the collection, analyses, or interpretation of data; in the writing of the manuscript, or in the decision to publish the results.

AUTHOR CONTRIBUTIONS

Conceptualization, M. Medina; methodology, E. Anoz-Carbonell, M. Rivero, V. Polo, A. Velazquez-Camoy and M. Medina; formal analysis, E. Anoz-Carbonell, M. Rivero, V. Polo and M. Medina; investigation, E. Anoz-Carbonell and M. Rivero; data curation, E. Anoz-Carbonell and M. Medina; writing—original draft preparation, E. Anoz-Carbonell and M. Medina; writing—review and editing, E. Anoz-Carbonell and M. Medina; project administration, M. Medina; funding acquisition, M. Medina.

REFERENCES

1. Karthikeyan S, Zhou Q, Mseeh F, Grishin NV, Osterman AL, Zhang H. Crystal structure of human riboflavin kinase reveals a beta barrel fold and a novel active site arch. *Structure*. 2003;11:265-273.
2. Karthikeyan S, Zhou Q, Osterman AL, Zhang H. Ligand binding-induced conformational changes in riboflavin kinase: structural basis for the ordered mechanism. *Biochemistry*. 2003;42:12532-12538.
3. Yazdanpanah B, Wiegmann K, Tchikov V, et al. Riboflavin kinase couples TNF receptor 1 to NADPH oxidase. *Nature*. 2009;460:1159-1163.
4. Hirano G, Izumi H, Yasuniwa Y, et al. Involvement of riboflavin kinase expression in cellular sensitivity against cisplatin. *Int J Oncol*. 2011;38:893-902.
5. Chen X, Ji B, Hao X, et al. FMN reduces Amyloid-β toxicity in yeast by regulating redox status and cellular metabolism. *Nat Commun*. 2020;11:867.
6. Zou YX, Zhang XH, Su FY, Liu X. Importance of riboflavin kinase in the pathogenesis of stroke. *CNS Neurosci Ther*. 2012;18:834-840.
7. Hirano A, Braas D, Fu YH, Ptáček LJ. FAD regulates CRYPTOCHROME protein stability and circadian clock in mice. *Cell Rep*. 2017;19:255-266.
8. Capo-chichi CD, Guéant JL, Lefebvre E, et al. Riboflavin and riboflavin-derived cofactors in adolescent girls with anorexia nervosa. *Am J Clin Nutr*. 1999;69:672-678.
9. Capo-Chichi CD, Feillet F, Guéant JL, et al. Concentrations of riboflavin and related organic acids in children with protein-energy malnutrition. *Am J Clin Nutr*. 2000;71:978-986.
10. Lee SS, McCormick DB. Thyroid hormone regulation of flavocoenzyme biosynthesis. *Arch Biochem Biophys*. 1985;237:197-201.
11. Barile M, Giancaspero TA, Brizio C, et al. Biosynthesis of flavin cofactors in man: implications in health and disease. *Curr Pharm Des*. 2013;19:2649-2675.
12. Barile M, Brizio C, Valenti D, De Virgilio C, Passarella S. The riboflavin/FAD cycle in rat liver mitochondria. *Eur J Biochem*. 2000;267:4888-4900.
13. Lienhart WD, Gudipati V, Macheroux P. The human flavoproteome. *Arch Biochem Biophys*. 2013;535:150-162.
14. Patel MV, Chandra TS. Metabolic engineering of *Ashbya gossypii* for enhanced FAD production through promoter replacement of FMN1 gene. *Enzyme Microb Technol*. 2020;133:109455.
15. Yruela I, Arilla-Luna S, Medina M, Contreras-Moreira B. Evolutionary divergence of chloroplasts FAD synthetase proteins. *BMC Evol Biol*. 2010;10:311.
16. Herguedas B, Martinez-Julvez M, Frago S, Medina M, Hermoso JA. Oligomeric state in the crystal structure of modular FAD synthetase provides insights into its sequential catalysis in prokaryotes. *J Mol Biol*. 2010;400:218-230.
17. Bauer S, Kemter K, Bacher A, Huber R, Fischer M, Steinbacher S. Crystal structure of *Schizosaccharomyces pombe* riboflavin kinase reveals a novel ATP and riboflavin-binding fold. *J Mol Biol*. 2003;326:1463-1473.

18. Herguedas B, Lans I, Sebastián M, Hermoso JA, Martínez-Júlvez M, Medina M. Structural insights into the synthesis of FMN in prokaryotic organisms. *Acta Crystallogr D Biol Crystallogr*. 2015;71:2526-2542.
19. Sebastián M, Velázquez-Campoy A, Medina M. The RFK catalytic cycle of the pathogen *Streptococcus pneumoniae* shows species-specific features in prokaryotic FMN synthesis. *J Enzyme Inhib Med Chem*. 2018;33:842-849.
20. Sebastián M, Serrano A, Velázquez-Campoy A, Medina M. Kinetics and thermodynamics of the protein-ligand interactions in the riboflavin kinase activity of the FAD synthetase from *Corynebacterium ammoniagenes*. *Sci Rep*. 2017;7:7281.
21. Walsh CT, Wencewicz TA. Flavoenzymes: versatile catalysts in biosynthetic pathways. *Nat Prod Rep*. 2013;30:175-200.
22. Sebastián M, Lira-Navarrete E, Serrano A, et al. The FAD synthetase from the human pathogen *Streptococcus pneumoniae*: a bifunctional enzyme exhibiting activity-dependent redox requirements. *Sci Rep*. 2017;7:7609.
23. Matern A, Pedrolli D, Großhennig S, Johansson J, Mack M. Uptake and metabolism of antibiotics roseoflavin and 8-demethyl-8-aminoriboflavin in riboflavin-auxotrophic *Listeria monocytogenes*. *J Bacteriol*. 2016;198:3233-3243.
24. Marcuello C, Arilla-Luna S, Medina M, Lostao A. Detection of a quaternary organization into dimer of trimers of *Corynebacterium ammoniagenes* FAD synthetase at the single-molecule level and at the in cell level. *Biochim Biophys Acta*. 2013;1834:665-676.
25. Lans I, Seco J, Serrano A, et al. The dimer-of-trimers assembly prevents catalysis at the transferase site of prokaryotic FAD synthase. *Biophys J*. 2018;115:988-995.
26. Solovieva IM, Tarasov KV, Perumov DA. Main physicochemical features of monofunctional flavokinase from *Bacillus subtilis*. *Biochemistry (Mosc)*. 2003;68:177-181.
27. Sebastián M, Arilla-Luna S, Bellalou J, Yruela I, Medina M. The biosynthesis of flavin cofactors in *Listeria monocytogenes*. *J Mol Biol*. 2019;431:2762-2776.
28. Barile M, Giancaspero TA, Leone P, Galluccio M, Indiveri C. Riboflavin transport and metabolism in humans. *J Inherit Metab Dis*. 2016;39:545-557.
29. Giancaspero TA, Colella M, Brizio C, et al. Remaining challenges in cellular flavin cofactor homeostasis and flavoprotein biogenesis. *Front Chem*. 2015;3:30.
30. Serrano A, Sebastián M, Arilla-Luna S, et al. The trimer interface in the quaternary structure of the bifunctional prokaryotic FAD synthetase from *Corynebacterium ammoniagenes*. *Sci Rep*. 2017;7:404.
31. Serrano A, Frago S, Herguedas B, Martinez-Julvez M, Velazquez-Campoy A, Medina M. Key residues at the riboflavin kinase catalytic site of the bifunctional riboflavin kinase/FMN adenylyltransferase from *Corynebacterium ammoniagenes*. *Cell Biochem Biophys*. 2013;65:57-68.
32. Vogt AD, Di Cera E. Conformational selection or induced fit? A critical appraisal of the kinetic mechanism. *Biochemistry*. 2012;51:5894-5902.
33. Frago S, Velázquez-Campoy A, Medina M. The puzzle of ligand binding to *Corynebacterium ammoniagenes* FAD synthetase. *J Biol Chem*. 2009;284:6610-6619.
34. Martinez-Julvez M, Abian O, Vega S, Medina M, Velazquez-Campoy A. Studying the allosteric energy cycle by isothermal titration calorimetry. *Methods Mol Biol*. 2012;796:53-70.
35. Velázquez-Campoy A, Goñi G, Peregrina JR, Medina M. Exact analysis of heterotropic interactions in proteins: Characterization of cooperative ligand binding by isothermal titration calorimetry. *Biophys J*. 2006;91:1887-1904.
36. Vega S, Abian O, Velazquez-Campoy A. A unified framework based on the binding polynomial for characterizing biological systems by isothermal titration calorimetry. *Methods*. 2015;76:99-115.
37. Olsson MHM, Søndergaard CR, Rostkowski M, Jensen JH. PROPKA3: consistent treatment of internal and surface residues in empirical pKa predictions. *J Chem Theory Comput*. 2011;7:525-537.
38. Delano WL. PyMOL: an open-source molecular graphics tool. *CCP4 Newsletter Pro Crys*. 2002;40:82-92.
39. Abraham MJ, Murtola T, Schulz R, et al. GROMACS: High performance molecular simulations through multi-level parallelism from laptops to supercomputers. *SoftwareX*. 2015;1-2:19-25.
40. Duan Y, Wu C, Chowdhury S, et al. A point-charge force field for molecular mechanics simulations of proteins based on condensed-phase quantum mechanical calculations. *J Comput Chem*. 2003;24:1999-2012.
41. Humphrey W, Dalke A, Schulten K. VMD: visual molecular dynamics. *J Mol Graph*. 1996;14:33-38, 27-38.
42. Lee SS, McCormick DB. Effect of riboflavin status on hepatic activities of flavin-metabolizing enzymes in rats. *J Nutr*. 1983;113:2274-2279.
43. Pedrolli DB, Nakanishi S, Barile M, et al. The antibiotics roseoflavin and 8-demethyl-8-amino-riboflavin from Streptomyces davawensis are metabolized by human flavokinase and human FAD synthetase. *Biochem Pharmacol*. 2011;82:1853-1859.
44. Jin C, Yao Y, Yonezawa A, et al. Riboflavin transporters RFVT/SLC52A mediate translocation of riboflavin, rather than FMN or FAD, across plasma membrane. *Biol Pharm Bull*. 2017;40:1990-1995.
45. Bollen YJ, Westphal AH, Lindhoud S, van Berkel WJ, van Mierlo CP. Distant residues mediate picomolar binding affinity of a protein cofactor. *Nat Commun*. 2012;3:1010.
46. Martínez-Júlvez M, Medina M, Velázquez-Campoy A. Binding thermodynamics of ferredoxin:NADP+ reductase: two different protein substrates and one energetics. *Biophys J*. 2009;96:4966-4975.
47. Yamada Y, Merrill AH Jr, McCormick DB. Probable reaction mechanisms of flavokinase and FAD synthetase from rat liver. *Arch Biochem Biophys*. 1990;278:125-130.
48. Torchetti EM, Bonomi F, Galluccio M, et al. Human FAD synthase (isoform 2): a component of the machinery that delivers FAD to apo-flavoproteins. *FEBS J*. 2011;278:4434-4449.
49. Sebastián M, Anoz-Carbonell E, Gracia B, et al. Discovery of antimicrobial compounds targeting bacterial type FAD synthetases. *J Enzyme Inhib Med Chem*. 2018;33:241-254.
50. Serrano A, Ferreira P, Martínez-Júlvez M, Medina M. The prokaryotic FAD synthetase family: a potential drug target. *Curr Pharm Des*. 2013;19:2637-2648.

SUPPORTING INFORMATION

Additional Supporting Information may be found online in the Supporting Information section.

How to cite this article: Anoz-Carbonell E, Rivero M, Polo V, Velázquez-Campoy A, Medina M. Human riboflavin kinase: Species-specific traits in the biosynthesis of the FMN cofactor. *The FASEB Journal*. 2020;34:10871–10886. https://doi.org/10.1096/fj.202000566R